OPEN ACCESS

University of BRISTOL

Isleifson, D., Galley, R. J., Firoozy, N., Landy, J. C., & Barber, D. G. (2018). Investigations into Frost Flower Physical Characteristics and the C-Band Scattering Response. *Remote Sensing*, *10*(7), [991]. https://doi.org/10.3390/rs10070991

Publisher's PDF, also known as Version of record

License (if available):
CC BY

Link to published version (if available):
10.3390/rs10070991

Link to publication record in Explore Bristol Research
PDF-document

This is the final published version of the article (version of record). It first appeared online via MDPI at https://doi.org/10.3390/rs10070991 . Please refer to any applicable terms of use of the publisher.

University of Bristol - Explore Bristol Research
General rights

This document is made available in accordance with publisher policies. Please cite only the published version using the reference above. Full terms of use are available:
http://www.bristol.ac.uk/red/research-policy/pure/user-guides/ebr-terms/

remote sensing

MDPI

Article

Investigations into Frost Flower Physical Characteristics and the C-Band Scattering Response

Dustin Isleifson [1,2,*], Ryan J. Galley [2], Nariman Firoozy [2], Jack C. Landy [3] and David G. Barber [2]

[1] Department of Electrical and Computer Engineering, University of Manitoba, Winnipeg, MB R3T 5V6, Canada
[2] Centre for Earth Observation Science, University of Manitoba, Winnipeg, MB R3T 5V6, Canada; Ryan.Galley@umanitoba.ca (R.J.G.); n.firoozy@gmail.com (N.F.); David.Barber@umanitoba.ca (D.G.B.)
[3] Bristol Glaciology Centre, University of Bristol, Bristol BS8 1HB, UK; Jack.Landy@bristol.ac.uk
* Correspondence: Dustin.Isleifson@umanitoba.ca; Tel.: +1-204-474-6553

Received: 9 May 2018; Accepted: 19 June 2018; Published: 22 June 2018

Abstract: A dedicated study on the physical characteristics and C-band scattering response of frost-flower-covered sea ice was performed in an artificial sea ice mesocosm over a 36-h period in January 2017. Meteorological conditions were observed and recorded automatically at the facility when the sea ice grew and frost flowers formed while the C-band scattering measurements were conducted continuously over a range of incidence angles. Surface roughness was characterized using a LiDAR. During the experiment, frost flowers did not initially form on the extremely smooth ice surface even though suitable meteorological conditions prevailed during their development (low air temperature, low near-surface wind speed, and high near-surface relative humidity). This provides evidence that both the presence of (i) liquid brine at the surface and (ii) raised nodules as nucleation points are required to enable frost flower initiation. As the ice thickened, we observed that raised nodules gradually appeared, frost flowers formed, and flowers subsequently spread to cover the surface over a six-hour period. In contrast to previous experiments, the frost flower layer did not become visibly saturated with liquid brine. The C-band scattering measurements exhibited increases as high as 14.8 dB (vertical polarization) in response to the frost flower formation with low incidence angles (i.e., 25°) showing the largest dynamic range. Co-polarization ratios responded to the physical and thermodynamic changes associated with the frost flower formation process. Our results indicate that brine expulsion at the sea ice surface and frost flower salination can have substantial temporal variability, which can be detected by scatterometer time-series measurements. This work contributes towards the operational satellite image interpretation for Arctic waters by improving our understanding of the highly variable C-band microwave scattering properties of young sea ice types.

Keywords: radar; microwave; scatterometer; LiDAR; Arctic; sea ice; frost flowers; surface roughness; NRCS

1. Introduction

The Arctic icescape is transitioning from a persistent cover of multi-year sea ice to predominantly first-year ice [1–3]. Along with this transition to thinner ice, sea ice mobility is increasing [4,5], which results in the potential for more frequent lead openings in sea ice during the winter season [4]. Frost flowers are a transient phenomenon that occur on newly-forming sea ice, which have received increased attention in recent years due to their influence on physical, radiative, and biogeochemical characteristics of the ocean-sea ice-atmosphere interface [6].

Frost flowers are fragile ice crystals that may grow into different structural forms depending on the atmospheric and boundary layer conditions that are present during their initial formation [7]. Thermodynamically, they act as an insulating layer at the ice-atmosphere boundary, which modifies the heat and radiative fluxes and influences the sea ice growth rate [8]. They also exhibit very high bulk salinity, which is thought to be caused by liquid brine being wicked up from a skim on the underlying sea ice surface. They continue to be the subject of field studies by atmospheric chemists. For example, Hara et al. [9] recently evaluated the presence of sea salts, frost flowers, atmospheric aerosol particles, and proposed sea-salt cycles. Frost flowers have also received attention for their role as a potential microbial habitat [10] and their impact on carbon cycling, which the newly-forming sea ice provides as a source of CO_2 to the atmosphere [11].

Certain atmospheric conditions near the surface and in the far-field favor the initiation and growth of frost flowers on new sea ice [12–14]. Micrometeorological conditions that favor frost flower formation include a large temperature difference between the relatively warm, newly-forming sea ice surface and the cold "far-field" atmosphere (e.g., where the "far-field" indicates the temperature at a theoretically infinitely large distance from the ice-atmosphere interface imposed as a boundary condition [12]). Additionally, frost flowers may grow when a low near-surface wind speed permits a water vapor pressure gradient to form between the surface (saturated air with respect to water) to a "far-field" height from the surface (sub-saturated). The low wind speeds and laminar surface flow preserves the shape of that gradient above the surface [14].

While the above micrometeorological conditions favor widespread frost flower initiation and spatial proliferation, they are not sufficient for producing frost flowers. Previous work [7,13,14] indicated that frost flowers require a vapor source, such as a liquid brine skim on the sea ice surface developed due to brine expulsion, which creates evaporative conditions at the surface due to super-saturation at the air-liquid brine skim interface. Galley et al. [14] further observed that mm-scale surface nodules are raised above the mean sea ice surface with lower surface temperatures than the brine skim surface, which induced frost flower initiation by providing condensation points for the supersaturated near-surface air. This agrees with the suggestions of Reference [15]. Once frost flower crystals have formed, high salinity brine on the sea ice surface is subsequently wicked up into the frost flower structure. The formation, growth, and eventual decay of frost flowers is a transient event that occurs over a time frame of 12 h to 48 h based on previous research [13,14,16,17].

Microwave remote sensing is used to monitor and evaluate thermodynamic and physical changes in sea ice from a local scale to a hemispheric scale [17,18]. Physically, sea ice is a complex, inhomogeneous substance consisting of a pure ice background embedded with brine and air inclusions. Its surface can be electromagnetically rough and/or covered with a layer of snow or frost flowers. Microwave propagation and scattering in sea ice are governed by the dielectric properties of the constituent materials, the size and shape of inclusions, and interface roughness. Since the dielectric constants of liquid brine and seawater are substantially greater than pure ice, the presence of liquid greatly influences electromagnetic wave interaction with the bulk material. Changes in the physical state due to environmental forcing affect the dielectric constant, which allows microwave scattering measurements to be linked to changes in the sea ice thermo-physical state.

Frost flowers have been the subject of remote sensing studies at scales ranging from satellite to on-site Arctic and laboratory studies under controlled conditions [19,20]. However, the ephemeral nature of frost flower initiation and growth has made a cross-comparison for scaling the lab and field studies to the satellite level quite challenging. The formation of frost flowers on sea ice results in an increase in microwave backscatter at C-band. This has been documented by field studies (e.g., a difference of 6 dB for frost flower covered sea ice versus bare sea ice [17]). Some of the earlier discussions and analysis of scattering from frost flowers on sea ice are summarized and presented in References [21,22]. Laboratory studies and mesocosm studies have demonstrated the increase in the backscatter as a function of frost flower formation on sea ice (e.g., increase of 6 dB, [20]). From a satellite perspective, previous analysis of ERS-1 synthetic aperture radar (SAR) C-band backscatter

showed increases of 5–10 dB [23] and 10–15 dB [24] when frost flowers appeared. Further progression of the backscattering values is highly dependent upon environmental conditions (e.g., wind, snowfall) and sea ice dynamics [24]. In a recent campaign focused on newly-forming sea ice (including frost flowers in Arctic leads), satellite-based SAR measurements at L-band, C-band, and X-band data were studied [25]. They suggested that L-band, due to greater penetration depth and lower sensitivity to surface structures, could be more useful than the C-band and X-band scenes for identifying regions of frost flowers [26].

Previous work at our sea ice mesocosm known as the Sea-ice Environmental Research Facility (SERF) showed that a near-surface based C-band polarimetric radar system could identify several stages of frost flower growth and development [19]. In the experiment, frost flower initiation resulted in a major increase in backscatter for all incidence angles and polarizations. Brine expulsion covering the sea ice surface with liquid was clearly captured by the radar data as a local minimum in the time-series scattering. The experiment continued with a local backscatter maximum followed by a slight decrease of backscatter as the frost flowers size and the areal coverage increased. A final stage of frost flower decimation (i.e., collapse and coalescence) was only identifiable in the backscatter results at low incidence angles (25°) where the co-polarization ratio reached near unity.

Recognizing that rapid changes in the thermodynamic and physical state of the surface were the primary causes of observed scattering behavior of frost-flower-covered sea ice (e.g., [19]), we planned our experiment to occur during atmospheric and sea ice physical conditions that would be conducive to frost flower growth. The overarching objective of this paper is to present the results from our experiment in January 2017 at SERF, which focused on the observation and analysis of the physical processes and C-band scattering characteristics of a frost-flower-covered sea ice surface over a 36-h period. Throughout this work, we compare and contrast the physical and microwave backscattering evolution of frost flowers of this second dedicated experiment with results from Reference [19] by highlighting the differences in the processes, frost flower formation, and scattering behavior. Specifically, we address the following three objectives.

(i) Describe and quantify the physical characteristics of frost-flower-covered sea ice during this experimental time period by focusing on improving our understanding of the physical mechanisms of frost flower development.
(ii) Measure and evaluate the temporal evolution of C-band scattering characteristics of a newly-formed sea ice surface that eventually became covered in frost flowers, which is physically and electromagnetically different from a bare sea ice surface.
(iii) Examine the link between the temporally evolving sea ice and frost flower physical properties with the measured scattering response.

The physical characteristics of a frost-flower-covered sea ice surface and the C-band scattering response elucidated in this paper are a step towards understanding the processes and variability at a small scale (i.e., mesocosm study). Moreover, environmental conditions may vary both seasonally and regionally. Therefore, exploration of the variability in frost flower formation and their effects on sea ice microwave scattering responses is required to improve satellite image interpretation for polar environmental monitoring applications. With the improved temporal resolution of satellite constellation missions (e.g., the Radarsat Constellation Mission (RCM), and Sentinel-1, which are designed to operate in C-band), the time-series data collected in this experiment are opportune.

2. Materials and Methods

2.1. Description of Facility

The SERF mesocosm consists of an outdoor pool at the University of Manitoba that measures 9.1 m (north-south) by 18.2 m (east-west) with a depth of 2.45 m (Figure 1). The pool contained artificial seawater, which was chemically formulated to replicate the ionic composition, alkalinity, and pH of the

natural Arctic Ocean surface water based on Reference [27] with a salinity of 34.9 practical salinity units (PSU). The pool is equipped with a series of heaters and pumps used to maintain an ice-free surface at sub-zero temperatures and/or counterclockwise water circulation as well as a retractable Quonset-style domed roof, which can enclose the entire pool. Further details of SERF are available elsewhere [19,27]. During the experiment, automated meteorological and surface measurement instrumentation were set up on the east half of the pool (as described in Section 2.2) while the west half of the pool remained physically undisturbed for radar and LiDAR measurements.

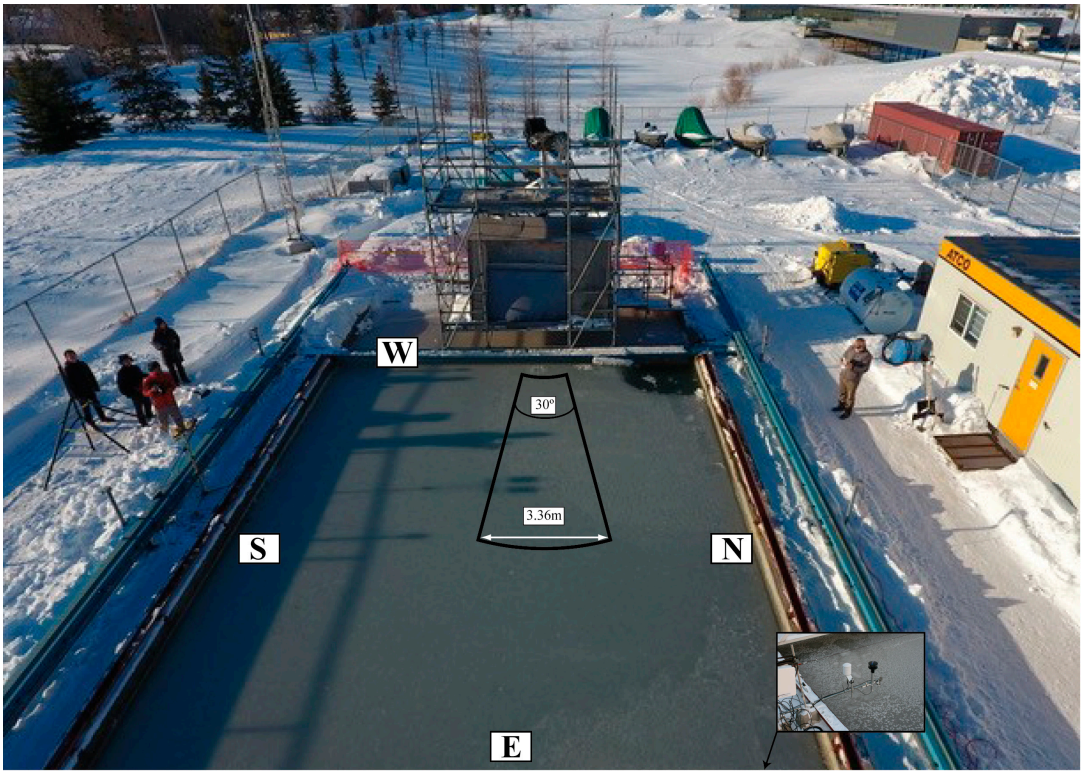

Figure 1. The SERF pool located on the University of Manitoba campus. The C-band scatterometer was mounted on the west side of the pool (showed in a stowed protected configuration at the end of the experiment). The LiDAR is located within the protected area beneath the scatterometer. Inset shows the automated meteorological equipment.

2.2. Physical Measurements

Near-surface (h = 70 cm) meteorological measurements included air temperature and relative humidity (Vaisala HMP45C, temperature accuracy = ±0.4 °C, relative humidity accuracy = ±2%) as well as wind speed and direction (Gill WindSonic Anemometer, wind speed accuracy = ±2% at 12 m/s, direction accuracy = ±3% at 12 m/s). The surface temperature of the seawater and later sea ice was measured remotely using an Apogee SI-111 infrared sensor (calibration uncertainty = 0.02 °C, measurement repeatability <0.05 °C). Ice and seawater temperatures were measured vertically at 2-cm intervals (top 32 measurements) and then at 5-cm increments from 65 cm to 190 cm. Then it was measured at 10-cm increments to the bottom of the pool using Type-T 24AWG thermocouples (special-limits-of-error, specified deviation of 0.1 °C over 1000′ of wire, Omega Inc., St-Eustache, QC, Canada). The thermocouples were mounted in a polyvinyl chloride pipe suspended into the water from a taught aircraft cable running across the pool (N-S) above the surface. The surface of the sea ice formed in the pool at the level of the fourth thermocouple from the top of our vertical array.

Frost flowers were carefully sampled from the sea ice using a pre-cleaned plastic spatula and placed into sterilized Whirl-Pak water-tight bags for measuring salinity in the lab. Scrapings of

the ice surface were formed for measuring salinity using a smooth stainless steel edge and placed into sterilized Whirl-Pak water-tight bags. Bulk samples of the newly-formed sea ice volume were extracted using a thin Japanese-style rip/crosscut saw and stored in Whirl-Pak bags to melt at room temperature. Physical samples were taken in triplicate (with one exception for the first frost flower samples). The conductivity and temperature of the melt of each sample were measured using a conductivity meter (Thermo Scientific Orion Star A212, Fisher Scientific Company, Ottawa, ON, Canada). The sample salinities were calculated from the conductivity, according to the formulation of Fofonoff [28]. We used Kimwipes® (a disposable, high-quality tissue paper) to detect surface wetness by touching the tissue to the surface and observing if any liquid was picked up by the fabric.

2.3. LiDAR Measurements

A Leica Scanstation C10 Light Detection and Ranging (LiDAR) system provided measurements of the centimeter-scale roughness of the ice surface. The scanner was mounted on a tripod and positioned on a platform directly beneath the scatterometer at a height of 2.1 m above the sea ice surface. Surface roughness data were acquired over a coincident area to radar backscatter measurements. The LiDAR was configured to emit pulses at a frequency of 50 kHz and to record the time-of-flight for each of the pulses reflected by the ice and received by the scanner. The system operates at a wavelength of 532 nm, so laser pulses are consistently reflected by surfaces, such as snow and ice, but are absorbed by water [29].

The raw scan included outlying points located well above or below the true pool surface, which are caused by laser reflections from precipitation and were removed using algorithms based on the morphological and adaptive triangular irregular network (TIN) filters of References [30,31], respectively. A series of 0.5 m × 0.5 m square sections were extracted from the LiDAR scan along the azimuthal swath of each scatterometer incidence angle from 20° to 45°. Each section was aligned to the direction of the scatterometer to coincide with the radar footprints as closely as possible. LiDAR points within each subsection were resampled to a regular grid made up of 2 mm × 2 mm cells using linear interpolation. Minor large-scale topography at the ice surface (caused by slight spatial variations in sea ice growth rates) was removed through spectral decomposition of the roughness power spectral density (PSD) and filtering out topography with a lateral wavelength >0.5 m. Two statistical measures of surface roughness: (i) root mean square (RMS) height (h) and (ii) correlation length (L_c) of deviations from a mean level through the grid were calculated for each subsection based on the algorithms of Reference [32]. The initial results were then calibrated using the functions provided in Reference [33], which accounted for bias introduced by the high inclination scanning angle of the LiDAR sensor to produce precise and accurate surface roughness parameters. Single parameters were estimated for each incidence angle of the scatterometer by averaging all subsections along a swath. Values for the RMS height and correlation length varied by less than 1 mm and 5 mm, respectively, between subsections along each scatterometer swath.

2.4. Radar Measurements

A C-band polarimetric scatterometer (center frequency = 5.5 GHz, bandwidth = 500 MHz, ProSensing, Inc., Amherst, MA, USA) measured the microwave scattering response of the sea ice throughout the experiment. The antenna is a dual-polarized reflector with a beam width of approximately 5.5° in both the E-plane and H-plane. It was mounted on a scaffolding tower platform directly above the LiDAR, which is 5.1 m above the seawater surface. Measurements were conducted with 30° swaths in azimuth and elevation incidence angles were set at discrete increments of 5° from 20° to 55° from nadir. The estimated number of independent samples ranged from n = 11 at 20° to n = 33 at 55°. The returned power was measured and the covariance matrix was calculated to allow the VV, HV, and HH normalized radar cross sections (NRCS) and polarimetric parameters to be obtained. When processing the scatterometer data on a per scan basis, we carefully ensured that the peak scattering was clearly identified (i.e., ensuring that a sufficient signal-to-noise ratio was

maintained), which is discussed in Reference [17]. The data collected from a trihedral corner reflector were utilized for measurement calibration and an internal delay line calibration monitored system drift during the experiment via periodic sky calibrations. The manufacturer-tested sensitivity of the instrument is -40 dB m^2/m^2 at a range of 15 m. In the processing of our time-series scatterometer data, we applied a moving average filter (n = 4) to better present the trend of the measured NRCS data. This system has been used in numerous field campaigns and its utility and processing were discussed in References [17,34,35]. Although all polarimetric data were collected, this manuscript focuses on the NRCS and their connections to the physical phenomenon observed in the SERF. Therefore, details on the polarimetric discriminants will be preserved for future work.

3. Results and Discussion

3.1. Stage I: Initial Sea Ice Growth

The experiment started on 12 January after the roof had been retracted and the heaters and pumps were turned off at 20:40. Water vapor gradually rose from the water surface at the experimental start time. Frazil ice began to accumulate in the SERF almost immediately. A continuous sea ice surface formed shortly before 23:00 (12 January). The sky was clear, the air temperature was <−25 °C, and the surface wind speed was very low (<1 m/s) (Figure 2). The air temperature decreased overnight and reached a minimum of −32.4 °C at 05:18 before slowly increasing. The cold overnight air temperature cooled the near-surface volume during the first 12 h of growth (Figure 2b) with the surface temperature reaching a minimum of −14.9 °C at 06:54. The air-surface temperature difference (i.e., $T_{surface}$–T_{air}, where positive values indicate a warmer surface overlain by colder air) ranged between 17 °C and 27 °C until about 06:00 on 13 January when it steadied around 15 °C. The near-surface wind speed stayed very low throughout the night until 06:00 (13 January) when it began to increase marginally (Figure 2). Physical sampling during this stage occurred overnight at 22:40 (12 January), and at 00:40 (13 January), and 04:40 (13 January). At 22:40 on 12 January, the initial dark nilas sea ice surface grew extremely smooth and remained dry. A Kimwipe® was unable to pick up any liquid from the surface. At 04:40 on 13 January, the sea ice was 2.7 cm thick with a bulk salinity of 22.3 PSU (Figures 3 and 4) and the surface was dry again. Frost flower coverage increased from a few sparse flowers at 04:40 to about 10% areal coverage by 07:40 (Figure 5). Although the micrometeorological conditions show that frost flower formation might have been expected during this initial sea ice growth period (i.e., strong temperature gradient and low wind speed), two physical factors were absent, which negated frost flower initiation. Liquid brine was absent from the sea ice surface throughout the overnight period so the near-surface air lacked a water vapor source to saturate it and the sea ice surface was exceptionally smooth and void of any raised nodules that might have served as relatively cold condensation points (compared to the mean ice surface). Photographic inspection (Figure 5) indicated the absence of raised nodules on the surface of the sea ice during this period. In this case, the absence of frost flowers supports the necessity of these physical factors for frost flower formation previously postulated in References [12,14].

NRCS measurements started at 23:00 on 12 January with the first appearance of a continuous, spatially consistent sea ice surface. Scatterometer measured backscatter at the C-band was low for all polarizations (Figure 6) during the initial sea ice formation before midnight on 12 January, which is expected considering the sea ice surface formed as a smooth sheet and remained mirror smooth while the ice thickened downwards into the water column [17]. From the initial measurements at 23:00 on 12 January to 08:40 on 13 January throughout the overnight initial ice growth stage of the experiment, the co-polarized (VV and HH) scattering magnitudes did not change substantially for the lowest incidence angles (25°) while a minor oscillation was observed for the cross-polarized scattering coefficient when the sea ice thickness increased. At moderate incidence angles (35° and 45°), we observed some oscillation for all polarizations when the ice thickened. The C-band scattering time-series collected during this initial sea ice growth stage followed a similar evolution to previous work on newly-formed, thickening sea ice (low backscatter, gradual increase with thickness, cross-polarized

backscattering was much lower than co-polarized backscattering) [19,36]. The co-polarization ratio (VV/HH) increased with an increasing incidence angle, which is typical for thin ice types [36].

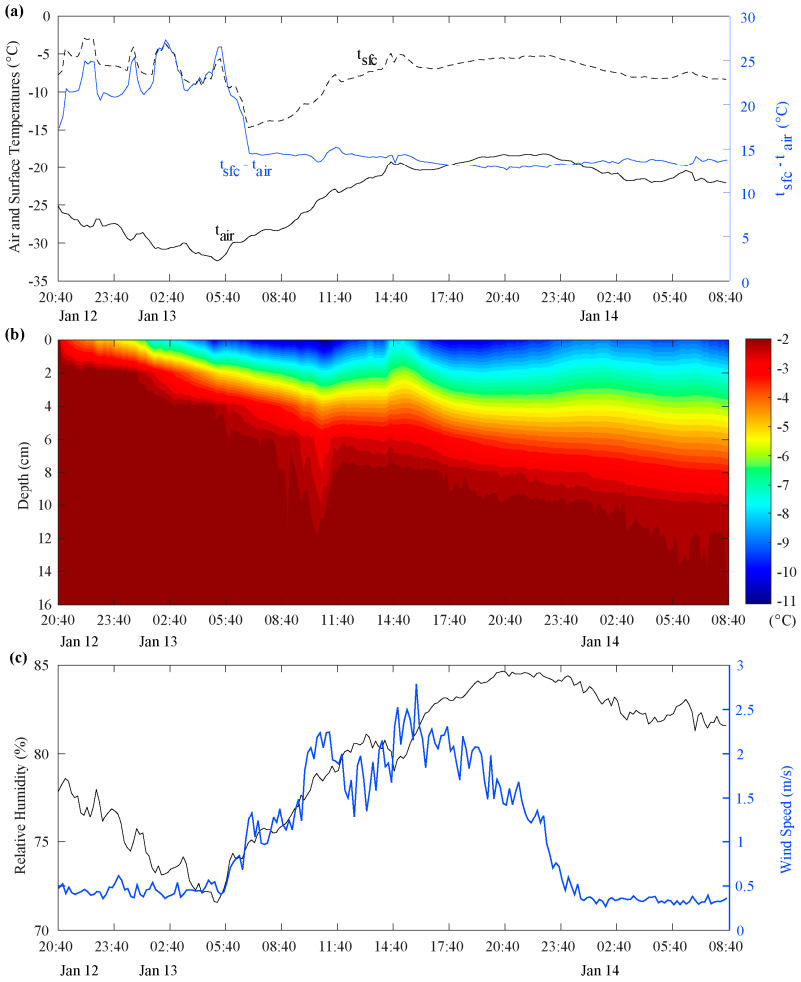

Figure 2. Measured environmental conditions. (**a**) Temperature (air and surface); (**b**) thermocouple profile in the sea ice; (**c**) relative humidity and wind speed.

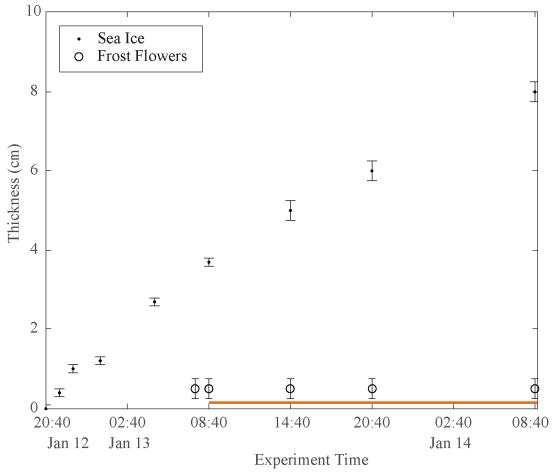

Figure 3. Measured sea ice thickness and frost flower heights. Surface liquid brine presence indicated by solid horizontal bar starting at 8:40 a.m.

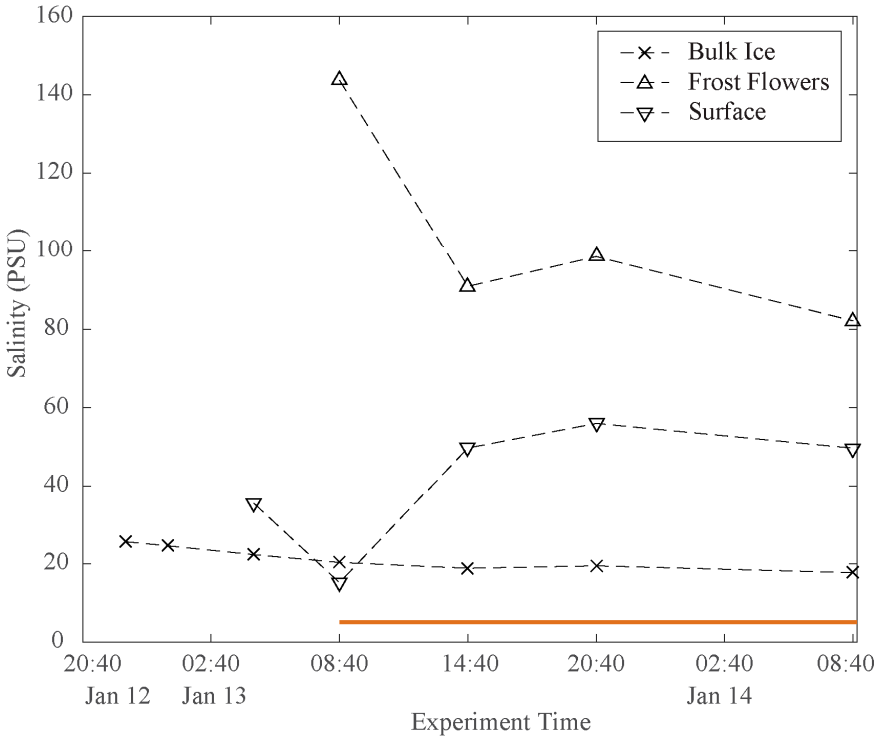

Figure 4. Mean salinity measurements during the experiment for bulk sea ice, frost flowers, and the sea ice surface. Surface liquid brine presence indicated by solid horizontal bar starting at 08:40.

Figure 5. The sea ice surface at 07:40 on 13 January prior to sunrise.

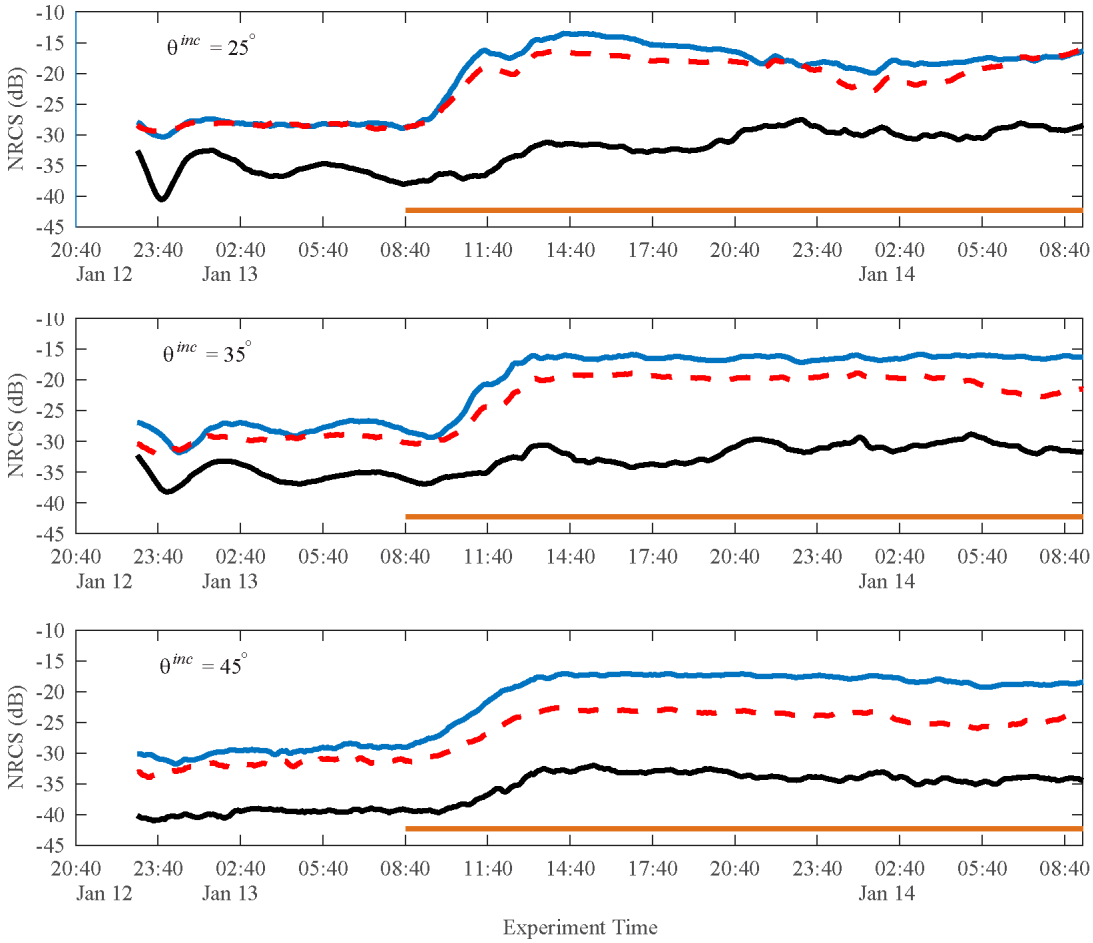

Figure 6. Backscatter measurements during the process of frost flower development for incidence angles from 25° to 45°. Polarizations are indicated as VV (solid blue), HH (dashed red), and HV (solid black). The solid horizontal yellow bar indicates when brine was present on the sea ice surface.

3.2. Stage 2: Initial Frost Flower Formation and Spatial Proliferation

Beginning on the morning of 13 January, widespread frost flower formation occurred and their proliferation proceeded spatially from 10% coverage in the morning to cover ~70% of the ice surface by mid-afternoon (14:40 on 13 January). This significant change in the characteristics of the newly-formed sea ice surface resulted from changes in the physical properties of the sea ice and micrometeorological variables, which is reflected in changes of the NRCS time series data until 14:40 on 13 January.

The initiation of rapid frost flower growth (04:40 on 13 January) was immediately followed by a three-hour period (05:40 to 08:40) during which the surface temperature declined rapidly from −5 °C to −15 °C before stabilizing at its minimum level for the experiment. Frost smoke was observed above the newly-formed sea ice surface at 05:40. The near-surface wind speed increased after 06:00 (Figure 2), which, in combination with the brine expulsion, began to roughen the previously extremely smooth sea ice surface. With observed frost smoke indicating evaporation of liquid at the surface, frost flowers began to form via the typical mechanism [12,14]. At 08:40 on 13 January, the ice thickness had reached 3.7 cm with a bulk salinity of 20.3 PSU. A Kimwipe® was gently touched to the surface and liquid indicated that the sea ice surface was brine-wetted at this point. The presence of liquid brine on the sea ice surface is indicated in Figures 2 and 4 by the solid horizontal orange bar in each panel. Frost flowers sampled at 08:40 were saline with heights of 5 ± 1 mm and surface coverage remained ~10%. Differential air-surface temperature plateaued at 15 °C for the remainder of the experiment with the surface temperature time series closely following the air temperature for the remaining duration.

The maximum near surface wind speed during this widespread frost flower proliferation stage was 2 m/s, with a mean of 1.74 m/s (Figure 2c), and did not vary much. The relative humidity 70 cm above the surface of the ice remained high (mean = 79% during this period). The sky was overcast for a few hours (approximately 12:00 noon to 14:00) and the sea ice temperature remained stable when the ice continued to grow thicker (Figure 2b). By 13:40, the ice thickness had reached 5 cm and had a bulk salinity of 18.9 PSU (Figures 3 and 4) and the sea ice surface below the frost flowers remained brine-wetted. After 14:00, the temperature of the surface and the ice volume warmed and then cooled again (Figure 2b), which corresponded to direct illumination of the surface by solar radiation for a few hours after 14:00. The surface salinity had increased to 49.8 PSU at 14:40 on 13 January (by a factor of 3.3 since 08:40). At 14:40, the bottom 2–3 mm of the frost flowers (still 5 mm tall) was still immersed in a brine-wetted layer and their bulk salinity was 90.9 PSU (including the brine-wetted portions). The depth of the brine-wetted layer was measured at multiple points within the physical sampling area using a ruler.

Frost flower salinities observed in this experiment were comparable with frost flower salinities in the literature (see Figure 4) and were always greater than the observed sea ice surface salinity, which indicates that there was a concentration of salt and other impurities upwards into the frost flowers. Frost flower salinities measured here were much larger than a previous SERF experiment [19], which indicates substantial variability in this process. Other frost flower salinity measurements include those by Martin et al. [16] (52 to 107 PSU), Isleifson et al. [17] (21.5 to 62.5 PSU), and Roscoe et al. [37] (95 ± 42 PSU). In this experiment, we observe that the frost flower salinity was twice as large as the surface salinity during frost flower growth. This can be observed in our experimental data as well as data sets from Reference [19] and Reference [20] while Martin et al. [16] noted that the salinity of the sea ice surface brine skim layer was around 1.4 times smaller than their observed frost flower salinity.

Scatterometer measurements during the period of significant frost flower spatial proliferation through the morning and early afternoon on 13 January indicate that the observed physical changes in the surface caused substantial increases in backscatter for all polarizations and incidence angles (Figure 6) with more pronounced increases at lower incidence angles. As the frost flowers grew and spatially covered the sea ice, NRCS increases by 14.8 dB (VV), 11.7 dB (HH), and 6.0 dB (HV) and were measured at 25°. Similar increases were observed for co-polarized signals at higher incidence angles. However, the cross-polarized trend lagged temporally. Liquid brine (first observed on the sea ice surface at 08:40 and then throughout this stage of the experiment) had a higher dielectric constant than the previously observed dry sea ice surface. The increase in permittivity results in an increase of the co-polarization ratio (VV/HH). This effect is more pronounced at higher incidence angles (Figure 6). Minimum backscatter occurred around 12:30 for co-polarized signals at 25°. Similar inflections were observed at other incidence angles and polarizations. However, they were not distinct minima similar to the 25° case. For comparison, at 25° incidence, Nghiem et al. reported an initial sea ice backscatter of −26 dB (VV), −28 dB (HH), and −34 dB (HV) before observing a substantially smaller increase of about 5 dB for VV and HH polarizations during frost flower growth and spatial proliferation. For HV, Nghiem et al. observed an initial decrease of 4 dB with a subsequent increase of 9 dB [20].

Figures 7 and 8 show images of the frost-flower-covered sea ice surface from a top view and an oblique view, respectively. LiDAR measurements at 14:30 on 13 January near the end of Stage 2 are shown in Figure 9 underlying the scatterometer scan footprint on the SERF pool surface and processed for the areas of the surface corresponding to scatterometer swaths at each incidence angle (Table 1). All aspects of the surface roughness (including the autocorrelation function (ACF) and anisotropy in L_c with the azimuth angle have been characterized with the LiDAR data [32]. The average RMS height (h) for individual incidence angles ranged from 0.23 cm to 0.26 cm and the correlation length (L_c) ranged from 0.57 cm to 0.99 cm. Maps of the correlation length and RMS height are given in Figure 9a,b.

RMS height showed very little variation ($\leq$0.3 mm) between scatterometer incidence angles. L_c exhibited some variation with a maximum value of 0.99 cm at 40° and a minimum value of 0.68 cm at a 20° scatterometer incidence angle. The surface is, therefore, electromagnetically rough (per the Rayleigh roughness criteria), which indicates that surface scattering will be present in the backscattering signatures. Figure 9 emphasizes that, in spite of similarities between RMS height at each incidence angles, there was inhomogeneity in the surface roughness that can be linked to the frost flower coverage. The roughness values we measured are in agreement with our previously reported values in Reference [19], which means that the geometric properties of the frost flowers were similar in both experiments. The LiDAR's capability for characterizing the frost flower roughness parameters is consistent between experiments.

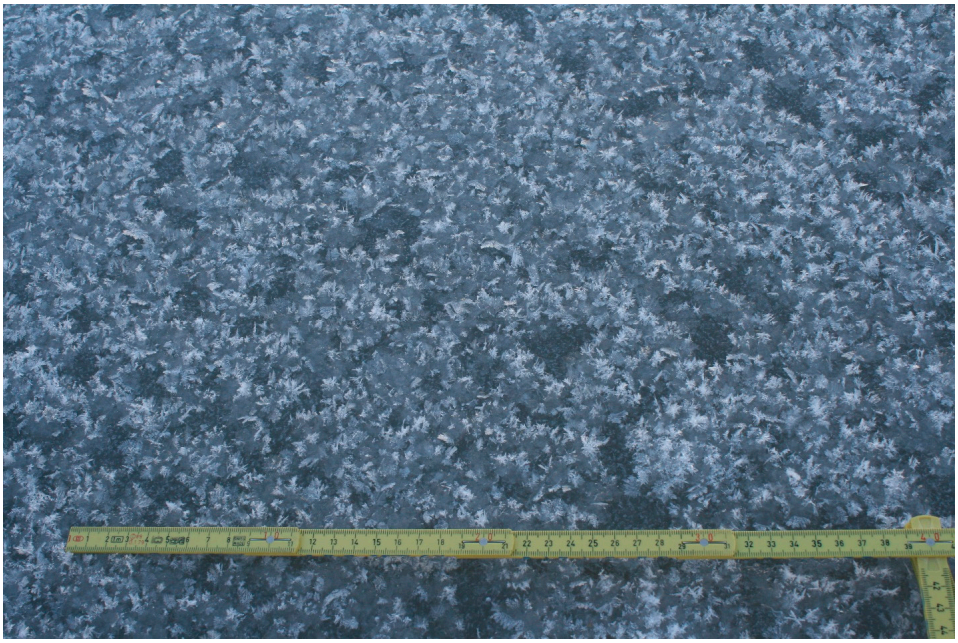

Figure 7. The sea ice surface at mid-afternoon showing dense frost flower growth (14:40 on 13 January).

Figure 8. Oblique view of the sea ice surface during the mid-afternoon. Bare ice patches are visible between frost flowers (14:40 on 13 January).

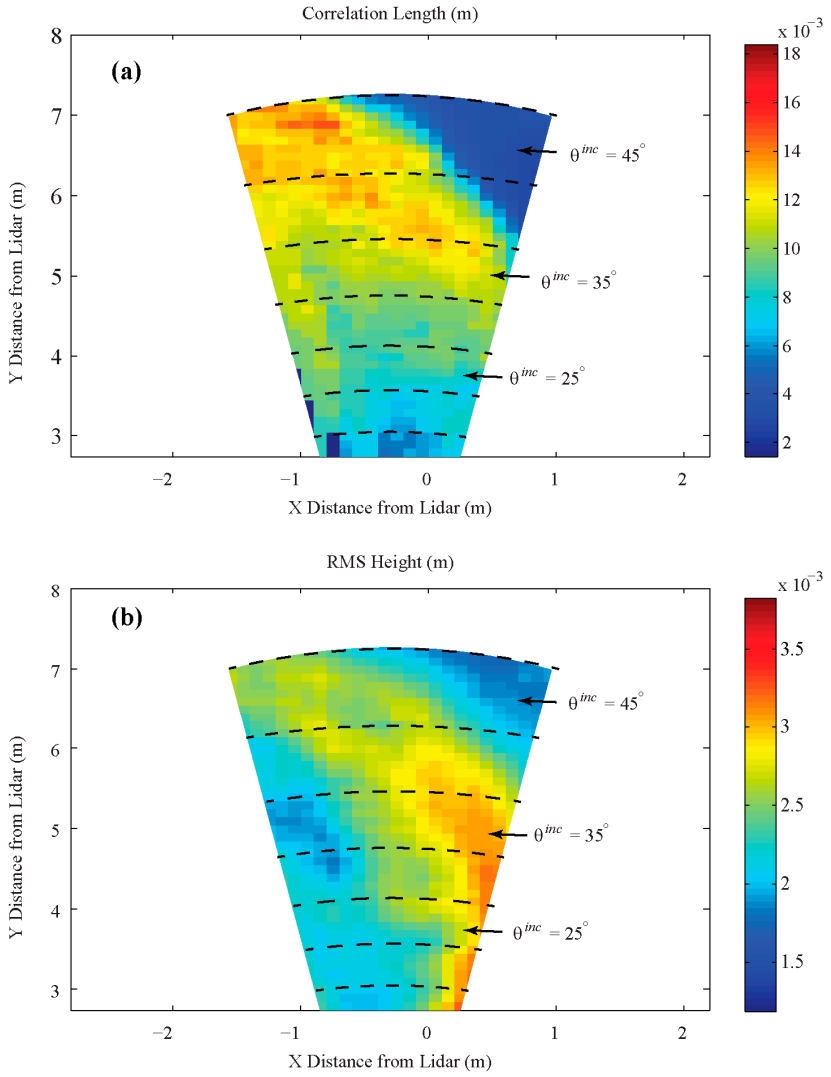

Figure 9. LiDAR Roughness Parameters. (**a**) Correlation Length and (**b**) Root Mean Square Height.

Table 1. Evaluated surface roughness parameters derived from LiDAR measurements.

Incidence Angle (°)	h (cm)	L_c (cm)
20	0.23	0.68
25	0.23	0.72
30	0.26	0.80
35	0.25	0.90
40	0.26	0.99
45	0.25	0.80

3.3. Late Stage

During the third stage of this experiment, from 14:40 on 13 January to 08:40 on 14 January, the sea ice surface was covered with frost flowers (Figures 7 and 8) that were no longer developing vertically or increasing in spatial coverage. Kimwipe® tests indicated that the sea ice surface was still brine-wetted during this stage.

From 14:40 to 20:40 on 13 January, the air and surface temperature marginally increased by 1–2 °C (Figure 2). Near surface wind speed remained low (mean wind speed for the six-hour period was 2.07 m/s) and the relative humidity increased from 80% to 85%. For a short period of time

(approximately from 14:40 to 15:40), the sun directly illuminated the sea ice surface, which accounts for the brief temperature increase in the air, sea ice surface, and sea ice volume temperatures over that hour (Figure 2).

At 20:40 on 13 January, the average height of the frost flowers remained 5 mm (Figure 3), the frost flower bulk salinity was 98.5 PSU (Figure 4), and the morphology had not substantially changed. A Kimwipe® was able to pick up liquid brine from the surface. The surface salinity had increased to 56 PSU, the sea ice thickness reached 6 cm, and the bulk sea ice salinity was 19.5 PSU.

Overnight, from 20:40 on 13 January to 08:40 on 14 January, the air and surface temperatures decreased and near surface wind speed decreased to 0.58 m/s and remained ~0.5 m/s for the remainder of the experiment (Figure 2). The sea ice temperature in the upper portion of the sea ice slightly increased in the evening as a result of energy accumulated at the surface during the daylight hours and then followed the cooling trend of the atmosphere (Figure 2).

At 08:40 (sunrise) on 14 January, we observed that the frost flowers were a mix of stellar dendritic and hexagonal plate crystals. The surface salinity had decreased to 49.7 PSU and the frost flower salinity had decreased to 82 PSU. The lower part of the frost flowers were brine-wetted, which was distinct from the underlying solid sea ice. This portion was included in the frost flower samples. The average sea ice thickness was 8 cm. Observations of the sea ice crystal structure showed that the upper 2 cm were randomly oriented crystals, consistent with the frazil ice growth, which was followed by a 1 cm transition layer (both of which are indicative of extremely quiescent growth conditions) and a 5 cm layer of congelation growth.

Scatterometer measurements exhibited differences throughout this time-period (i.e., 14:40 on 13 January to experiment end), which is dependent upon the incidence angle (see Figure 6). For 25° incidence angle, the co-polarized backscatter decreased from 14:40 on 13 January to 00:40 on 14 January with a commensurate increase in cross-polarized backscatter. The co-polarized ratio reached approximately unity from 21:00 to 23:00 on 13 January. This is coincident to the maximum air temperature, surface temperature, and relative humidity. Assuming that surface roughness did not change appreciably during this short time, these results suggest that volume scattering was enhanced. In reality, the scattering process is very complex since the sea ice surface roughness and underlying ice may also contribute to backscatter. At 00:40 on 14 January, the co-polarized backscatter reached a local minimum for a 25° incidence angle and increased, which reached a local maximum at the end of the experiment. From 05:40 on 14 January to the end of the experiment, the co-polarized ratio was <1 dB. Physical measurements showed that the lower part of the frost flowers were brine-wetted at this time.

At 35° incidence, the co-polarized backscatter remained stable (steady within ±1 dB) from 14:40 on 13 January to 02:40 on 14 January while the cross-polarized backscatter had an increase and some fluctuations (~5 dB). The co-polarized backscatter (HH) reached a local minimum at 06:40 on 14 January, which was followed by an increase toward the end of the experiment. The co-polarized VV backscatter remained steady from about 13:40 on January 13 to the end of the experiment.

For 45° incidence, the co-polarized backscatter remained stable (steady within ±0.5 dB) from 14:40 on 13 January to 01:40 on 14 January while the cross-polarized backscatter had a gradual decrease and some fluctuations (~2 dB). Overnight, the co-polarized backscatter (both VV and HH) decreased slightly, which reached a local minimum at 06:40 on 14 January followed by an increase toward the end of the experiment.

Major fluctuations were not observed in the C-band backscatter results in Stage 3, which is consistent with results from our previous experiment [19]. The sea ice surface frost flower spatial coverage and vertical heights did not change measurably during Stage 3, which indicates the C-band scatterometer measurements were responding primarily to thermodynamic changes. In evaluating the surface coverage from LiDAR data and photographs, the surface was not uniformly covered with frost flowers. Therefore, direct comparison of results at different incidence angles is complex. Based on our results (Figure 6), the lowest incidence angles (i.e., 25°) are the most sensitive to the changes in frost flower coverage, physical changes, and thermodynamic effects. This agrees with our

previous assessment in Reference [19]. Moreover, we have shown that the co-polarized ratio at the 25° incidence angle provides additional information that is not readily apparent from the individual co-polarized channels.

4. Conclusions

We investigated the C-band scattering signatures and physical properties of frost-flower-covered sea ice at the SERF located at the University of Manitoba. We presented and analyzed physical characteristics, which evaluated the measured scattering response at multiple incidence angles of the C-band and examined how the physical characteristics of an evolving sea ice surface eventually covered in frost flowers gave rise to its scattering response over time.

The sea ice surface was initially extremely smooth and devoid of a liquid brine skim during Stage 1 of this experiment and consequently frost flowers were not formed despite theoretically appropriate meteorological conditions (low air temperature, low near-surface wind speed, and high near-surface relative humidity). This provides evidence for the presence of (i) liquid brine at the surface and (ii) raised nodules as nucleation points potentially enabling frost flower initiation. Frost flowers began to form when we observed frost smoke due to brine expulsion. The surface temperature decreased rapidly to its minimum for the experimental period upon a marginal increase in the near-surface wind speed. A liquid brine skim was observed on the surface of the sea ice while the frost flower coverage increased. The formation of frost flowers and their subsequent coverage of the sea ice surface occurred over the six hours directly following these observed changes at the surface. The sea ice surface salinity increased by more than a factor of three.

The C-band NRCS measurements substantially increased, which coincided with the appearance of the liquid brine skim and subsequent frost flower formation at the surface. We observed a minor short-term minimum NRCS at 25° incidence as the lower layers of the frost flowers became brine-soaked and the sea ice surface salinity rapidly increased. The effect was less distinct with higher incidence angles. Our measurements indicate that the brine expulsion phase and frost flower salinization can have substantial temporal variability (i.e., there are differences between previous experiments [19] and this experiment), which can be detected by scatterometer time-series measurements. We can confirm that low incidence angles (25°) are most sensitive to physical and thermodynamic changes in frost flower covered sea ice. The observations and measurements of the delayed brine expulsion provide unique experimental data, which enhance our understanding of frost flowers and sea ice growth processes.

Further work is required to understand the timing of brine expulsion at the surface of the sea ice and its effects on frost flower growth processes and their ensuing salinization. In the future, evaluating surface roughness in advance of initial frost flower formation should occur to assess the development and effect of nucleation sites on the eventual initiation and proliferation of frost flowers. Polarimetric scattering measurements and their interpretation must be part of future experimental work. Contemporary satellite constellation missions are designed to obtain high spatial resolution imagery with higher revisit frequency than single satellites. However, the images are collected at a relatively low temporal resolution when compared to the rapid geophysical changes observed in this experiment. Therefore, the results from this high-temporal resolution remote sensing experiment can be used to interpret and predict the time-series microwave scattering signatures between satellite imaging operations, which are instrumental for understanding processes in the changing Arctic.

Author Contributions: D.I., R.J.G., and D.G.B. were responsible for the study conceptualization. D.I., R.J.G., N.F., and J.C.L. handled the methodology. D.I., R.J.G., N.F., and J.C.L. managed the software. D.I., R.J.G., N.F., and J.C.L. validated the results. D.I., R.J.G., N.F., and J.C.L. took part in formal analysis. D.I. and D.G.B. managed the resources. D.I. curated data. D.I. and R.J.G. wrote and prepared the original draft. D.I., R.J.G., N.F., J.C.L., and D.G.B. reviewed and edited the manuscript. D.I., D.G.B. supervised the project. D.I. and D.G.B. administered the project. Funding Acquisition, D.I., R.J.G., and D.G.B. acquired the funding.

Funding: The Canadian Foundation for Innovation (CFI) provided funding for the project infrastructure. Research was supported through the NSERC Discovery Grant program to D.I., D.G.B., and R.J.G. and Canada Research Chair (CRC) program grants to D.G.B.

Acknowledgments: The authors would like to thank the operations staff and fellow researchers at CEOS. Special thanks to the SERF technician D. Binne.

Conflicts of Interest: The authors declare no conflict of interest.

References

1. Kwok, R.; Cunningham, G.F.; Wensnahan, M.; Rigor, I.; Zwally, H.J.; Yino, D. Thinning and volume loss of the Arctic Ocean sea ice cover: 2003–2008. *J. Geophys. Res. Oceans* **2009**, *114*. [CrossRef]
2. Maslanik, J.J.; Stroeve, J.; Fowler, C.; Emery, W. Distribution and trends in Arctic sea ice age through spring 2011. *Geophys. Res. Lett.* **2011**, *38*. [CrossRef]
3. Galley, R.J.; Babb, D.; Ogi, M.; Else, B.G.T.; Geilfus, N.-X.; Crabeck, O.; Barber, D.G.; Rysgaard, S. Replacement of multiyear sea ice and changes in open water season duration in the Beaufort Sea since 2004. *J. Geophys. Res. Oceans* **2016**, *121*, 1806–1823. [CrossRef]
4. Rampal, P.; Weiss, J.M.D. Positive Trend in the Mean Speed and Deformation Rate of Arctic Sea Ice, 1979–2007. *J. Geophys. Res. Oceans* **2009**, *114*. [CrossRef]
5. Spreen, G.; Kwok, R.; Menemenlis, D. Trends in Arctic Sea Ice Drift and Role of Wind Forcing: 1992–2009. *Geophys. Res. Lett.* **2011**, *38*. [CrossRef]
6. Barber, D.G.; Ehn, J.K.; Pućko, M.; Rysgaard, S.; Deming, J.W.; Bowman, J.S.; Papakyriakou, T.; Galley, R.J.; Søgaard, D.H. Frost flowers on young Arctic sea ice: The climatic, chemical, and microbial significance of an emerging ice type. *J. Geophys. Res. Atmos.* **2014**, *119*, 11593–11612. [CrossRef]
7. Style, R.W.; Worster, M.G. Frost flower formation on sea ice and lake ice. *Geophys. Res. Lett.* **2009**, *36*. [CrossRef]
8. Martin, S.; Yu, Y.; Drucker, R. The temperature dependence of frost flower growth on laboratory sea ice and the effect of the flowers on infrared observations of the surface. *J. Geophys. Res. Oceans* **1996**, *101*, 12111–12125. [CrossRef]
9. Hara, K.; Matoba, S.; Hirabayashi, M.; Yamasaki, T. Frost flowers and sea-salt aerosols over seasonal sea-ice areas in northwestern Greenland during winter–spring. *Atmos. Chem. Phys.* **2017**, 8577–8598. [CrossRef]
10. Bowman, J.S.; Deming, J.W. Elevated bacterial abundance and exopolymers in saline frost flowers and implications for atmospheric chemistry and microbial dispersal. *Geophys. Res. Lett.* **2010**, *37*. [CrossRef]
11. Geilfus, N.-X.; Carnat, G.; Dieckmann, G.; Halden, N.; Nehrke, G.; Papakyriakou, T.; Tison, J.-L.; Delille, B. First estimates of the contribution of $CaCO_3$ precipitation to the release of CO_2 to the atmosphere during young sea ice growth. *J. Geophys. Res. Oceans* **2013**, *118*, 244–255. [CrossRef]
12. Notz, D.; Worster, G. Desalination processes of sea ice revisited. *J. Geophys. Res. Oceans* **2009**, *114*. [CrossRef]
13. Gallet, J.C.; Domine, F.; Savarino, J.; Dumont, M.; Brun, E. The growth of sublimation crystals and surface hoar on the Antarctic plateau. *Cryosphere* **2014**, *8*, 1205–1215. [CrossRef]
14. Galley, R.J.; Else, B.G.T.; Geilfus, N.X.; Hare, A.A.; Babb, D.; Papakyriakou, T.; Barber, D.G.; Rysgaard, S. Micrometeorological and thermal control of frost flower growth and decay on young sea ice. *Arctic* **2015**, *68*, 79–92. [CrossRef]
15. Perovich, D.; Richter-Menge, J. Surface Characteristics of Lead Ice. *J. Geophys. Res. Oceans* **1994**, *99*, 16341–16350. [CrossRef]
16. Martin, S.; Drucker, R.; Fort, M. A laboratory study of frost flower growth on the surface of young sea ice. *J. Geophys. Res. Oceans* **1995**, *100*, 7027–7036. [CrossRef]
17. Isleifson, D.; Hwang, B.; Barber, D.G.; Scharien, R.K.; Shafai, L. C-Band Polarimetric Backscattering Signatures of Newly Formed Sea Ice During Fall Freeze-Up. *IEEE Trans. Geosci. Remote Sens.* **2010**, *48*, 3256–3267. [CrossRef]
18. Barber, D.G. Microwave remote sensing, sea ice and Arctic climate. *Phys. Can.* **2005**, *61*, 105–111.
19. Isleifson, D.; Galley, R.J.; Barber, D.G.; Landy, J.C.; Komarov, A.; Shafai, L. A Study on the C-band Polarimetric Scattering and Physical Characteristics of Frost Flowers on Experimental Sea Ice. *IEEE Trans. Geosci. Remote Sens.* **2014**, *52*, 1787–1798. [CrossRef]

20. Nghiem, S.V.; Martin, S.; Perovich, D.K.; Kwok, R.; Drucker, R.; Gow, A.J. A laboratory study of the effect of frost flowers on C-band radar backscatter from sea ice. *J. Geophys. Res. Oceans* **1997**, *102*, 3357–3370. [CrossRef]
21. Onstott, R.G. SAR and scatterometer signatures of sea ice. In *Microwave Remote Sensing of Sea Ice*; Carsey, F.D., Ed.; AGU: Washington, DC, USA, 1992.
22. Tucker, W.B.; Perovich, D.K.; Gow, A.J.; Weeks, W.F.; Drinkwater, M.R. Physical properties of sea ice relevant to remote sensing. In *Microwave Remote Sensing of Sea Ice*; Carsey, F.D., Ed.; AGU: Washington, DC, USA, 1992.
23. Ulander, L.M.H.; Carlström, A.; Askne, J. Effect of frost flowers, rough saline snow and slush on the ERS-1 SAR backscatter of the Arctic sea ice. *Int. J. Remote Sens.* **1995**, *16*, 3287–3305. [CrossRef]
24. Melling, H. Detection of features in first-year pack ice by synthetic aperture radar (SAR). *Int. J. Remote Sens.* **1998**, *19*, 1223–1249. [CrossRef]
25. Johansson, A.M.; King, J.A.; Doulgeris, A.P.; Gerland, S.; Singha, S.; Spreen, G.; Busche, T. Combined observations of Arctic sea ice with near-coincident colocated X-band, C-band, and L-band SAR satellite remote sensing and helicopter-borne measurements. *J. Geophys. Res. Oceans* **2017**, *122*, 669–691. [CrossRef]
26. Johansson, A.M.; Brekke, C.; Spreen, G.; King, J.A. X-, C-, and L-band SAR signatures of newly formed sea ice in Arctic leads during winter and spring. *Remote Sens. Environ.* **2018**, *204*, 162–180. [CrossRef]
27. Hare, A.A.; Wang, F.; Barber, D.; Geilfus, N.X.; Galley, R.J.; Rysgaard, S. pH evolution in sea ice grown at an outdoor experimental facility. *Mar. Chem.* **2013**, *154*, 46–54. [CrossRef]
28. Fofonoff, N.P. Physical properties of seawater: A new salinity scale and equation of state for seawater. *J. Geophys. Res. Oceans* **1985**, *90*, 3332–3342. [CrossRef]
29. Perovich, D.K. The Optical Properties of Sea Ice. In *Physics of Ice-Covered Seas*; Lepparanta, M., Ed.; Helsinki University Press: Helsinki, Finland, 1998; Volume 1, pp. 195–230.
30. Vosselman, G. Slope Based Filtering of Laser Altimetry Data. *Int. Arch. Photogramm. Remote Sens.* **2000**, *33*, 935–942.
31. Axelsson, P. DEM generation from laser scanner data using adaptive TIN models. *Int. Arch. Photogramm. Remote Sens.* **2000**, *33*, 110–117.
32. Landy, J.C.; Isleifson, D.; Komarov, A.S.; Barber, D.G. Parameterization of Centimeter-Scale Sea Ice Surface Roughness Using Terrestrial LiDAR. *IEEE Trans. Geosci. Remote Sens.* **2015**, *53*, 1271–1286. [CrossRef]
33. Landy, J.C.; Komarov, A.S.; Barber, D.G. Numerical and Experimental Evaluation of Terrestrial LiDAR for Parameterizing Centimeter-Scale Sea Ice Surface Roughness. *IEEE Trans. Geosci. Remote Sens.* **2015**, *53*, 4887–4898. [CrossRef]
34. Geldsetzer, T.; Mead, J.; Yackel, J.; Scharien, R.; Howell, S. Surface-Based Polarimetric C-Band Scatterometer for Field Measurements of Sea Ice. *IEEE Trans. Geosci. Remote Sens.* **2007**, *45*, 3405–3416. [CrossRef]
35. Firoozy, N.; Mojabi, P.; Landy, J.; Barber, D.G. Landfast First-Year Snow-Covered Sea Ice Reconstruction via Electromagnetic Inversion. *IEEE J. STARS* **2016**, *9*, 2414–2428. [CrossRef]
36. Nghiem, S.V.; Kwok, R.; Yueh, S.H.; Gow, A.J.; Perovich, D.K.; Kong, J.A.; Hsu, C.C. Evolution in polarimetric signatures of thin saline ice under constant growth. *Radio Sci.* **1997**, *32*, 127–151. [CrossRef]
37. Roscoe, H.K.; Brooks, B.; Jackson, A.V.; Smith, M.H.; Walker, S.J.; Obbard, R.W.; Wolff, E.W. Frost flowers in the laboratory: Growth, characteristics, aerosol, and the underlying sea ice. *J. Geophys. Res. Atmos.* **2011**, *116*. [CrossRef]

© 2018 by the authors. Licensee MDPI, Basel, Switzerland. This article is an open access article distributed under the terms and conditions of the Creative Commons Attribution (CC BY) license (http://creativecommons.org/licenses/by/4.0/).